

Direct Analysis of SANS and SAXS Measurements of Catanionic Surfactant Mixtures by Fourier Transformation

Daniel J. Iampietro, Laura L. Brasher,[†] and Eric W. Kaler*

Center for Molecular and Engineering Thermodynamics, Department of Chemical Engineering,
University of Delaware, Newark, Delaware 19716

Anna Stradner and Otto Glatter

Institut für Physikalische Chemie, Universität Graz, A-8010 Graz, Austria

Received: October 13, 1997; In Final Form: February 23, 1998

Vesicle and micellar structures formed by mixtures of the oppositely charged surfactants cetyltrimethylammonium bromide (CTAB) and sodium octyl sulfate (SOS) with and without added sodium bromide (NaBr) have been examined by small-angle neutron scattering (SANS) and small-angle X-ray scattering (SAXS) techniques. The resulting spectra have been evaluated using a Fourier transform/deconvolution technique. Through indirect Fourier transformation of the scattering intensity and subsequent deconvolution of the resulting cross-sectional pair distance distribution function, detailed information of the cross-sectional and interfacial dimensions of the aggregates is obtained. SANS and SAXS show that the vesicle bilayer has a core radius of 9 Å and a headgroup region extending an average 9 Å more. SANS results for the micelles investigated indicate a core radius of 10–11 Å and a headgroup region of 10 Å. This analysis, when compared with theoretical calculations from a thermodynamic cell model, indicates that the surfactant headgroups occupy a diffuse region near the core/water interface.

Introduction

Aqueous mixtures of oppositely charged surfactants form a wide variety of microstructures, ranging from highly curved micelles to flat lamellae, depending on the surfactant mixing ratio. Of particular interest is the spontaneous formation of an equilibrium phase of unilamellar vesicles,¹ and much work has been focused on determining the stability of these vesicles.^{2–5} Experimental observations show that the range of compositions over which vesicles form can be increased in a variety of ways, including increasing the asymmetry between the two surfactant tails⁶ or by branching of one of the surfactant chains.⁷ Conversely, adding a simple electrolyte destabilizes the vesicle phase.^{8–10}

Theories describe vesicle formation in terms of a balance between free energy contributions that favor and oppose aggregation. Since these vesicles are equilibrium structures, the aggregation of surfactant monomers to form vesicles must minimize the total free energy of the mixture. Molecular thermodynamic models^{6,11,12} have been developed using these principles to explore the effects of surfactant geometry and solution properties on the free energy of aggregation, thereby creating a greater understanding of microstructure formation in mixed surfactant systems.

One important experimental method for studying colloidal systems is small-angle scattering (SAS). In particular, small-angle neutron scattering (SANS) and small-angle X-ray scattering (SAXS) probe the pertinent colloidal length scales of 10–1000 Å. In addition, because the two kinds of scattered radiation

are sensitive to different physical properties of the scattering particle, these techniques can be used in parallel to obtain a rich variety of information.

The intensity of neutrons scattered from an aggregate is proportional to the difference in the neutron scattering length density between the aggregate and the solvent. Since the scattering length density is an intrinsic property of each nucleus, the average scattering length density of the aggregate is related to its composition. Contrast variation¹³ provides a powerful tool for determining the composition of colloidal aggregates because it takes advantage of the distinct scattering length densities of different atoms, particularly the large difference in scattering length density between hydrogen and deuterium. In comparison, the scattered intensity of X-rays is proportional to the difference of electron density between the aggregate and the solvent. The electron density is directly proportional to the number of electrons in an atom. In an ionic surfactant molecule, the hydrocarbon chains have comparatively fewer electrons than the headgroup, thus creating a large change in the electron density profile at the interface of the aggregate. Consequently, SAXS is particularly useful for investigating the interfacial region of aggregates composed of ionic surfactant molecules.

Previously, the phase behavior of mixtures of the oppositely charged surfactants cetyltrimethylammonium bromide (CTAB) and sodium octyl sulfate (SOS) with⁸ and without¹⁴ added salt has been studied. In the absence of added salt, a large vesicle region exists on the SOS-rich side of the phase diagram. The addition of screening electrolyte (5 wt % NaBr) to a sample containing 2 wt % of a 3/7 weight ratio mixture of CTAB and SOS destabilizes the vesicle phase and leads to the formation of a micellar phase. Calculations using a thermodynamic cell

* To whom correspondence should be addressed.

[†] Current address: Union Carbide Corporation, PO Box 670, Bound Brook, NJ 08805.

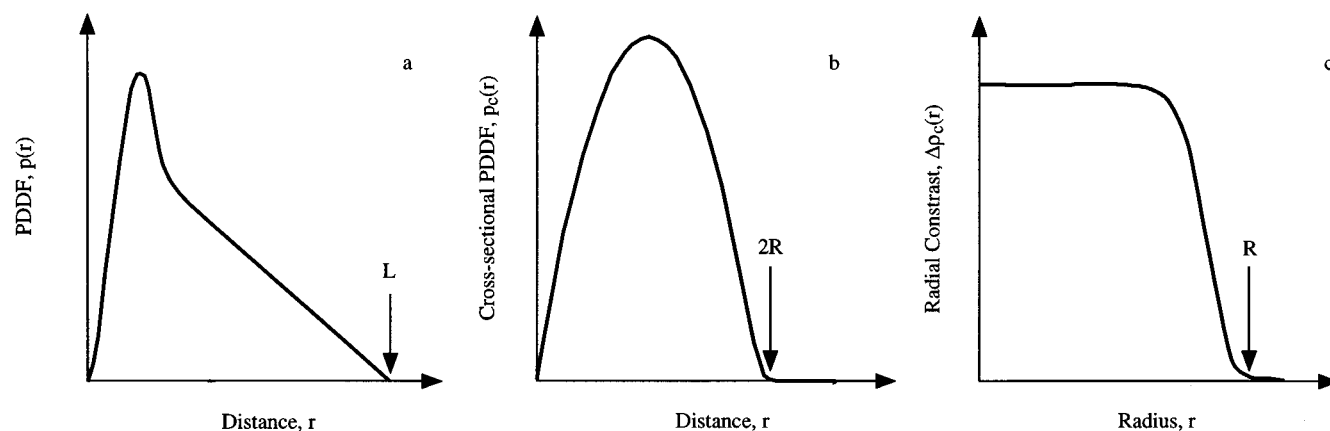


Figure 1. Schematic representations of the (a) PDDF, (b) cross-sectional PDDF, and (c) radial contrast profiles for a cylinder of diameter $2R$ and length L .

model indicate that the addition of salt favors an increase in the aggregation of the SOS monomers, thereby increasing the surface charge of the aggregate and creating a smaller, more curved micellar aggregate. Results of the cell model were verified by contrast variation SANS.¹⁵ In those experiments the low q SANS data were analyzed in the Guinier approximation to extract structural information about the aggregate. For the vesicle samples, the bilayer thickness was calculated to be 22 Å, which agrees exactly with the results of the cell model.

The development of a model-independent methodology^{16,17} for the analysis of small-angle scattering data provides a new pathway for obtaining more detailed information about the scattering particle. A combination of indirect Fourier transformation of the scattered intensity followed by a deconvolution of the resulting pair distance distribution function enables the determination of the local geometry, characteristic length scales, and scattering contrast profile of the particle while using little a priori knowledge about the aggregate. In this work, SANS and SAXS are used in parallel to study the structural changes occurring as cationic/anionic aggregates are transformed from vesicles to micelles with added salt. Analysis of the contrast profiles derived from the scattered intensity provides information about the internal and interfacial structure of the aggregates.

Theory

Indirect Fourier Transformation/Deconvolution. The methodology for analyzing small-angle scattering data using indirect Fourier transformation followed by a deconvolution technique has been described in detail elsewhere^{16,17} and recently outlined.^{18,19} The discussion here will only emphasize the main ideas, and the interested reader is referred to the original papers for a more in-depth description.

For a particle of arbitrary shape and scattering density difference, $\Delta\rho(\mathbf{r})$, the pair distance distribution function $p(r)$ (PDDF) for the particle is given by

$$p(r) = r^2 \tilde{\Delta\rho}^2(r) \quad (1)$$

where $\tilde{\Delta\rho}^2(r)$ is the convolution square of $\Delta\rho(\mathbf{r})$ averaged over all directions in space. This averaging is not necessary for the simplest case of a spherical particle where the neutron scattering length difference or electron density difference, $\Delta\rho_c(r)$, is only a function of the radial position. Here the subscript x refers to the shape of the particle ($x = s$ for a sphere, c for a cylinder, and t for a bilayer).

The PDDF is related to the scattered intensity $I(q)$ by the Fourier transformation

$$I(q) = 4\pi \int_0^\infty p(r) \frac{\sin(qr)}{qr} dr \quad (2)$$

with q the magnitude of the scattering vector \mathbf{q} defined as

$$q = \frac{4\pi}{\lambda} \sin\left(\frac{\theta}{2}\right) \quad (3)$$

where λ is the wavelength of the incident radiation and θ is the angle between the scattered and incident beam.

If the scattering objects (micelles) are cylindrical and $\Delta\rho_c(r)$ is only a function of the radial position within the cross section, the situation is similar to the one with spheres. The Fourier transformation of the intensity curve again yields the overall PDDF (see Figure 1a). The axial length of the cylinder is responsible for the linear region of $p(r)$ for large r , and the distance at which the PDDF decays to zero provides a measure of the length of the micelles. The slope of the linear portion is directly related to the square of the average contrast between the particle and solvent. If the cylinder is at least 3 times longer than the cross-sectional diameter, it is possible to study the radial structure of the micelle. The radial profile $\Delta\rho_c(r)$ is related to the PDDF for the cross section $p_c(r)$ by²⁰

$$p_c(r) = r \Delta\rho_c^2(r) \quad (4)$$

The cross section PDDF (Figure 1b) can be calculated from the scattered intensity via

$$I(q)q = \pi L I_c(q) = 2\pi^2 L \int_0^\infty p_c(r) J_0(qr) dr \quad (5)$$

where $J_0(qr)$ is the zero-order Bessel function. The indirect transformation of eq 5 yields $p_c(r)$ which is then used to calculate $\Delta\rho_c(r)$ (Figure 1c) via the deconvolution technique. Any radial inhomogeneity in $\Delta\rho_c(r)$ leads to a pronounced minimum in the PDDF in the region of $0 < r < 2R$.

The pair distance distribution functions for a vesicle (lamellar) structure are sketched in Figure 2. If the vesicles are monodisperse, oscillations in the PDDF are observed at large values of r . In most cases, though, the vesicles are polydisperse, and the oscillations are smeared out to give the PDDF shown in Figure 2a. The calculation of the scattering contrast profile for lamellar and unilamellar vesicles is similar to that for cylinders. Assuming that the contrast difference $\Delta\rho_c(r)$ within the bilayer

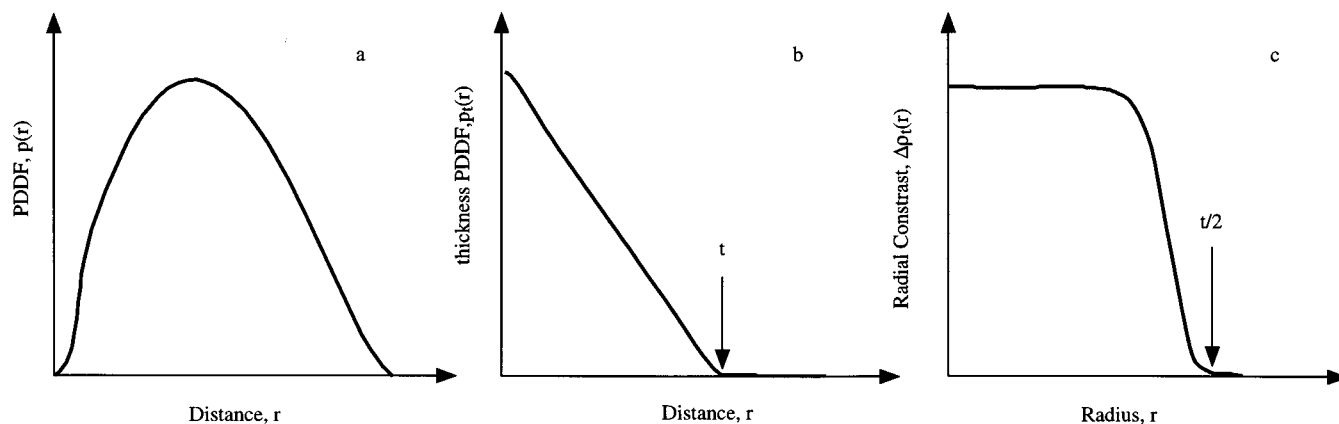


Figure 2. Schematic representations of the (a) PDDF, (b) cross-sectional PDDF, and (c) radial contrast profiles for a vesicle (lamellae) with bilayer thickness t .

core is only a function of the distance from the midplane, $\Delta\rho_t(r)$ can be evaluated. The thickness pair distance distribution function $p_t(r)$ (Figure 2b) is given by²⁰

$$p_t(r) = \Delta\bar{\rho}_t^2(r) \quad (6)$$

and the thickness PDDF is related to the scattered intensity of the thickness $I_t(q)$ by

$$I(q)q^2 = 2\pi A I_t(q) = 4\pi A \int_0^\infty p_t(r) \cos(qr) dr \quad (7)$$

The indirect transformation of eq 7 produces the thickness PDDF, which can be deconvoluted to obtain $\Delta\rho_t(r)$ (Figure 2c).

Cell Model. A thermodynamic cell model has been developed for the purpose of understanding the experimental observations and is described elsewhere in detail.^{6,11} In the cell model, the total free energy of aggregation for 1 mol of solution is minimized with respect to the parameters that adequately describe the size and composition of the putative geometry. For a vesicle geometry, these include the fraction of each surfactant aggregated, radius, bilayer thickness, fraction of surfactant molecules on the inner monolayer, and composition of the inner monolayer.

The free energy change upon aggregation for each trial of the parameters is calculated by summing the contributions favoring or opposing aggregation:

$$\Delta G_{\text{agg}} = G_{\text{hyd}} + G_{\text{el}} + G_{\text{int}} + G_{\text{st}} + G_{\text{ch}} + G_{\text{mix}} + G_{\text{entr}} \quad (8)$$

These represent, in order, the hydrophobic, electrostatic, interfacial, steric, chain packing, tail mixing (for two components), and entropic contributions to the total free energy of aggregation. Aggregate size and composition are determined by global minimization of the total Gibbs free energy of aggregation.

Experimental Section

Materials. The surfactant solutions for SANS experiments were made using D_2O as solvent (99.9% deuterated, low paramagnetic, low conductivity, from Cambridge Isotopes). Samples for the SAXS experiments were made with distilled and deionized H_2O (specific resistance was 18.3 $\text{M}\Omega \text{ cm}$). Sodium octyl sulfate (SOS, MW = 232.3) was obtained from Lancaster Synthesis and purified as a 10 wt % solution by the method of Rosen,²¹ using Waters Sep-Pak C_{18} cartridges. Some surfactant is lost in the cartridge during purification, so a two-phase titration assay is performed to determine the surfactant concentration.²² Cetyltrimethylammonium bromide (CTAB,

MW = 364.5) was obtained from Aldrich and was recrystallized three times in a 50:50 mixture of ethanol and acetone. Deuterated SOS (MW = 249.3) was synthesized by reacting deuterated 1-octanol (received from Cambridge Isotopes, 98% deuterated) with chlorosulfonic acid, followed by neutralization with sodium carbonate. The deuterated SOS product was extracted from the aqueous solution with 1-butanol, recrystallized twice in ethanol, and further purified as an 8% solution by Rosen's method.²¹ Sodium bromide (NaBr), purchased from Sigma, was oven-dried.

Sample Preparation. Stock solutions of each surfactant were prepared at various concentrations by precisely weighing the CTAB crystals or concentrated SOS (d-SOS) solution into glass bottles and then diluting to the desired surfactant concentration with D_2O or H_2O . Next, NaBr was weighed into scintillation vials and diluted to the appropriate NaBr weight percent with either CTAB or SOS (d-SOS) stock solution. Thus, salt concentration is on a total solution weight basis, whereas surfactant concentration is on a salt-free basis. The corresponding oppositely charged surfactant stock solutions were then mixed at the desired ratio. Adding salt to both stock solutions rather than as the last step eliminates any osmotic shocking of the vesicle phases.

SANS. SANS experiments were conducted at the research nuclear reactor at the National Institute of Standards and Technology in Gaithersburg, MD. The wavelength of radiation λ was 5 Å, with a spread in wavelength $\Delta\lambda/\lambda$ of 14%. Data were collected at detector (64 pixels \times 64 pixels, each pixel is 1 cm^2) distances of 1.0, 3.5, and 11.0 m from the sample. Samples were held in 2.0 mm thick quartz cells in a temperature-controlled sample chamber. SANS measurements were performed at 40 °C instead of 25 °C to offset the differences in hydrogen bonding between H_2O and D_2O . More than 10^6 counts were collected for every sample. The raw data were corrected for detector efficiency, scattering from the empty cell, and background radiation and placed on absolute scale using standards provided by NIST.

SAXS. SAXS experiments were performed in Graz using an X-ray generator (Philips, PW 1730/10) operating at 50 kV and 50 mA with a sealed tube Cu anode ($\text{K}\alpha$ wavelength of 1.54 Å). A Kratky compact camera equipped with a thermostated sample holder and a position-sensitive detector (MBraun, PSD-50M) with a metal wire was used. The resolution mode of the position-sensitive detector was 2k for all measurements with an effective total number of about 400 channels at a sample-to-detector distance of 217 mm (each channel corresponding to a spacing of $\sim 64 \mu\text{m}$). All experiments were

performed at 25 ± 0.5 °C. No monochromator was used, so the radiation contained Cu K α and about 25% K β radiation. The Kratky camera was operated with an entrance slit of 60 μ m. Sample and solvent were measured for $5 \times 15\,000$ s, leading to a total of about 10^8 counts for every sample. Raw data were corrected for detector efficiency variations. Data were not placed on an absolute scale.

Scattering Results

The primary results are the experimental SANS and SAXS curves. A quantitative numerical analysis of properly pretreated data (after correction of instrumental broadening from slit smearing in the Kratky camera and wavelength smearing for both X-rays and neutrons) involving model-independent inverse Fourier transformation provides information not previously available. Contrary to the typical procedure for the analysis of small-angle scattering data, the geometry is not assumed but is determined unambiguously from the pair distribution function $p(r)$ that is obtained from the inverse Fourier transformation of the scattering spectra. The only assumption in all types of such analysis is that of monodispersity, namely that all particles have the same size and shape. Knowledge of the geometry allows the appropriate convolution square root to be taken of the corresponding cross section distance distribution function. The final results are then the exact size or local length scale of the aggregates, and the detailed variation of the scattering length density (SANS) or electron density (SAXS) profiles $\Delta\rho_z(r)$ normal to the surface. It should be noted that vesicles made under both conditions were measured using X-rays, and the resulting distribution functions and density profile for the D₂O sample were not significantly different from those obtained in H₂O. Thus, changing temperature does not strongly influence the observed microstructure.

SANS. Experiments were performed for salt concentrations of 0.0 and 5.0 wt % NaBr. The solution composition for each salt concentration was 78 mM surfactant in D₂O (on a salt-free basis) and 21 mol % CTAB, a composition equivalent to 2.0 wt % 3/7 weight ratio CTAB/SOS in H₂O. This point is located near the center of the vesicle lobe with no added salt. For each salt concentration, the scattering contrast of the aggregate core was varied by using four different amounts of deuterated SOS (d-SOS) to make up the total SOS concentration. The fractions of d-SOS (f_{deut}) used were 0.25, 0.50, 0.75, and 1.00. In Figures 3 and 4, the scattering data are plotted as $I(q) - B$ where $I(q)$ is the total scattered intensity and B is the background calculated from the slope of a Porod plot (Iq^4 versus q^4).

Without Salt. Figure 3 shows a plot of $I(q) - B$ versus q for the four fractions of d-SOS. The top three curves have been offset by scale factors of 10, 100, and 1000, respectively, and for each sample a different intercept ($q \rightarrow 0$) was determined. The sample containing the least amount of d-SOS, and therefore having the greatest contrast with the solvent, has the largest $I(q \rightarrow 0)$ value prior to scaling. The intensities decay as q^{-2} for low values of q , characteristic of a lamellar-like structure such as dilute, polydisperse vesicles. For higher values of q , the finite thickness of the bilayer cross section causes the intensity to decay more rapidly. The solid line plotted along with the experimental data is the fit of the data obtained by Fourier transforming the PDDF in Figure 7a and smearing the resulting intensity spectra.

With Salt. Figure 4 shows a plot of $I(q) - B$ versus q for all four d-SOS compositions with the top three curves again offset by scale factors of 10, 100, and 1000, respectively, with the solid lines indicating the fit. The curves are qualitatively

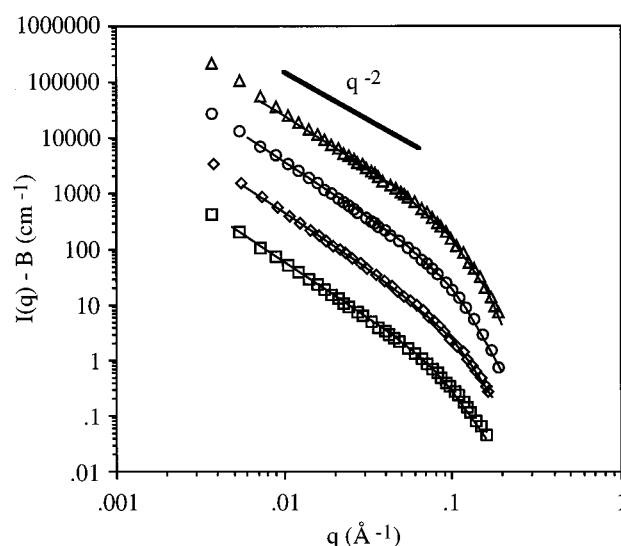


Figure 3. SANS results for the vesicle samples with no added salt. Scattered intensity vs q for the four d-SOS fractions with the top three curves offset by scale factors of 10, 100, and 1000, respectively. A slope of q^{-2} is indicated for comparison to the intensity at low values of q . The open symbols represent the experimental data and the solid lines the fit to the experimental data obtained by Fourier transformation of the PDDF in Figure 7a and subsequent smearing of the result. The fractions of d-SOS are 25% d-SOS (\square), 50% d-SOS (\diamond), 75% d-SOS (\circ), and 100% d-SOS (\triangle).

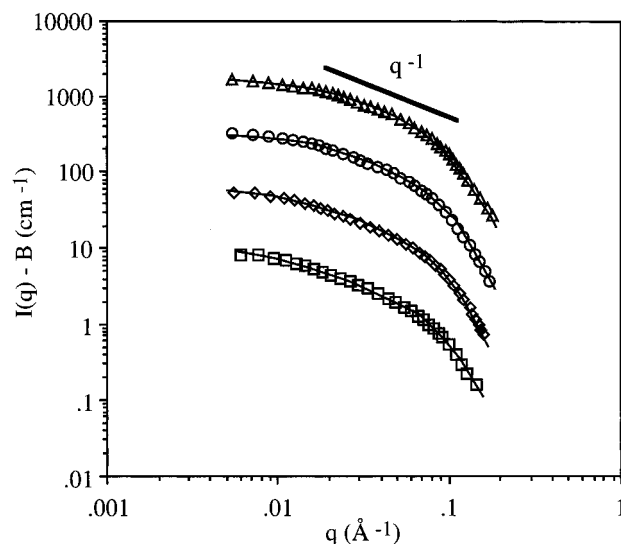


Figure 4. SANS results for the micelle samples with 5 wt % added salt. Scattered intensity vs q for the four d-SOS fractions with the top three curves offset by scale factors of 10, 100, and 1000, respectively. A slope of q^{-1} is indicated to highlight the region characteristic for scattering from rodlike aggregates. The open symbols represent the experimental data and the solid lines the fit to the experimental data obtained by Fourier transformation of the PDDF in Figure 7b and subsequent smearing of the result. The fractions of d-SOS are 25% d-SOS (\square), 50% d-SOS (\diamond), 75% d-SOS (\circ), and 100% d-SOS (\triangle).

different from those in Figure 3, indicating that the aggregates have a different structure. The intensity follows a q^{-1} dependence characteristic for cylindrical structures such as elongated micelles. The q^{-1} region is bounded at low q by the influence of the radius of gyration R_g on the scattering intensity and at high q by the cross-sectional dimension of the micelle core. For long micelles, R_g is much larger than the micelle diameter, and the q^{-1} region is extensive. For shorter micelles, such as those present here, R_g and the diameter are similar in magnitude,

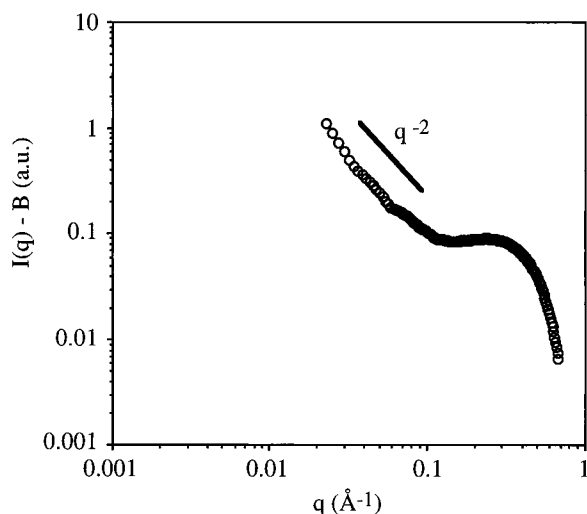


Figure 5. SAXS results for the vesicle sample with no added salt. Desmeared scattered intensity plotted vs q . A slope of q^{-2} is indicated for comparison to the intensity at low values of q .

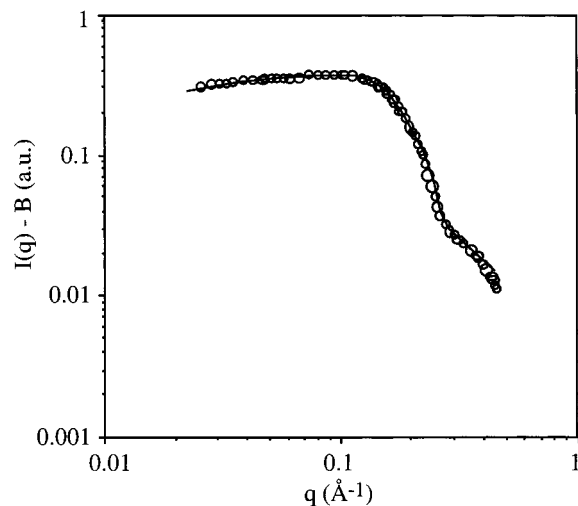


Figure 6. SAXS results for the micelle sample with 5 wt % NaBr plotted as the scattered intensity vs q . The solid line is the fit to the experimental data obtained by Fourier transformation of the PDDF in Figure 7d and subsequent smearing of the result. The agreement indicates the internal consistency of the routine.

and the q^{-1} region is small. The solid line indicates the fit obtained by Fourier transformation of the PDDF in Figure 7b.

SAXS. Small-angle X-ray scattering experiments were performed in parallel to the neutron scattering measurements at the salt concentrations and compositions (2 wt % 3/7 CTAB/SOS) indicated above. The samples for SAXS were prepared in H_2O instead of D_2O , and 100% hydrogenated SOS was used to make the total concentration of the anionic surfactant.

Without Salt. Due to the slit collimation of the X-ray beam, the intensity measured in the Kratky camera is distorted or smeared. Desmearing the experimental data corrects for slit smearing and yields the intensity that would be seen in the absence of these effects. Figure 5 shows the desmeared data plotted as $(I(q) - B)$ versus q . A region of q^{-2} dependence of the intensity exists at low q , and the sharp decay in intensity at high q is due to the thickness dimension of the bilayer. Undulations in the desmeared data are artifacts due to cutoff effects in the desmearing routine.

With Salt. Figure 6 displays a plot of $(I(q) - B)$ versus q for the sample containing 5 wt % NaBr. The shape of the spectra is qualitatively similar to that found by SANS (Figure

4). The slight maximum seen at $q \sim 0.1 \text{ Å}^{-1}$ should not be interpreted as an interaction peak (due to the low concentration of surfactant and screening of charges by salt), but is a consequence of the low overall scattering in the solution (see Numerical Analysis). As in Figures 3 and 4 the solid line represents the fit of the experimental data.

Numerical Analysis

Indirect Fourier Transformation. The first step in the analysis of the scattering data is the indirect Fourier transformation, which yields the pair distance distribution function (PDDF), $p(r)$. The most important information obtained from $p(r)$ is the geometry of the aggregate. The geometry is easily determined by comparing the PDDFs obtained from the scattering data to those calculated theoretically for a given geometry and contrast profile (Figures 1 and 2).

Figure 7a shows the $p(r)$ curves calculated for the SANS spectra measured for samples free of salt (Figure 3). The shape of the distribution functions in Figure 7a are all qualitatively similar to that pictured in Figure 2a for a locally flat particle. This result is expected for large polydisperse vesicles whose outer radius is much larger than the bilayer thickness. The $p(r)$ function for lamellar structures initially increases as r^2 but becomes linear in r at a distance corresponding to the thickness of the bilayer. For relatively thick lamellae or for lamellae with highly inhomogeneous density profiles (as is the case for the SAXS data here), the r^2 to r transition can be detected by eye. This is, however, hardly possible in the present case of homogeneous thin lamellar structures.²³ Figure 7b shows the $p(r)$ curves calculated from the SANS spectra measured for samples containing 5 wt % NaBr (Figure 4). A comparison of these distribution functions to that pictured in Figure 1a strongly supports the presumption of a locally cylindrical structure with a homogeneous density profile. The $p(r)$ functions of the micelles indicate a cylindrical shape and a maximum size of less than 400 Å. It should be noted, however, that excluded-volume effects can slightly reduce the apparent length of the cylindrical structures. If the cylinders are considerably longer than 400 Å, it would be important to consider flexibility and excluded-volume effects as well as other interparticle interactions in more detail.^{24,25} In our case the ratio between the length and the diameter of the cylinder is less than 10. For short cylinders there is not a well-developed q^{-1} dependence at low q .

Figure 7c shows the $p(r)$ curve calculated from the SAXS spectra without salt (Figure 5). The observed minima at $r < 50 \text{ Å}$ in $p(r)$ is a result of an inhomogeneous electron density profile. For higher values of r , the curve takes on a shape similar to Figure 7a, indicating a planar geometry. Figure 7d displays the $p(r)$ curve calculated from the SAXS spectra with 5 wt % NaBr (Figure 6). The presence of a minimum in $p(r)$ again indicates an inhomogeneous density profile. On the basis of the SANS results (Figures 4 and 7b), one would expect to see the long decay in $p(r)$ at large values of r . This feature is absent in the distribution function of Figure 7d. The slope of the long decay is proportional to the square of the average contrast between the aggregate and the solvent. The high level of electrolyte in the bulk solvent increases its electron density to a point where it effectively matches the average value for the aggregate. Matching the electron density of the aggregate to that of the solvent reduces the average contrast to approximately zero and thus drives $p(r)$ to zero for larger values of r . In this case, the $p(r)$ curve in Figure 7d provides no conclusive information about the overall structure of the aggregate.

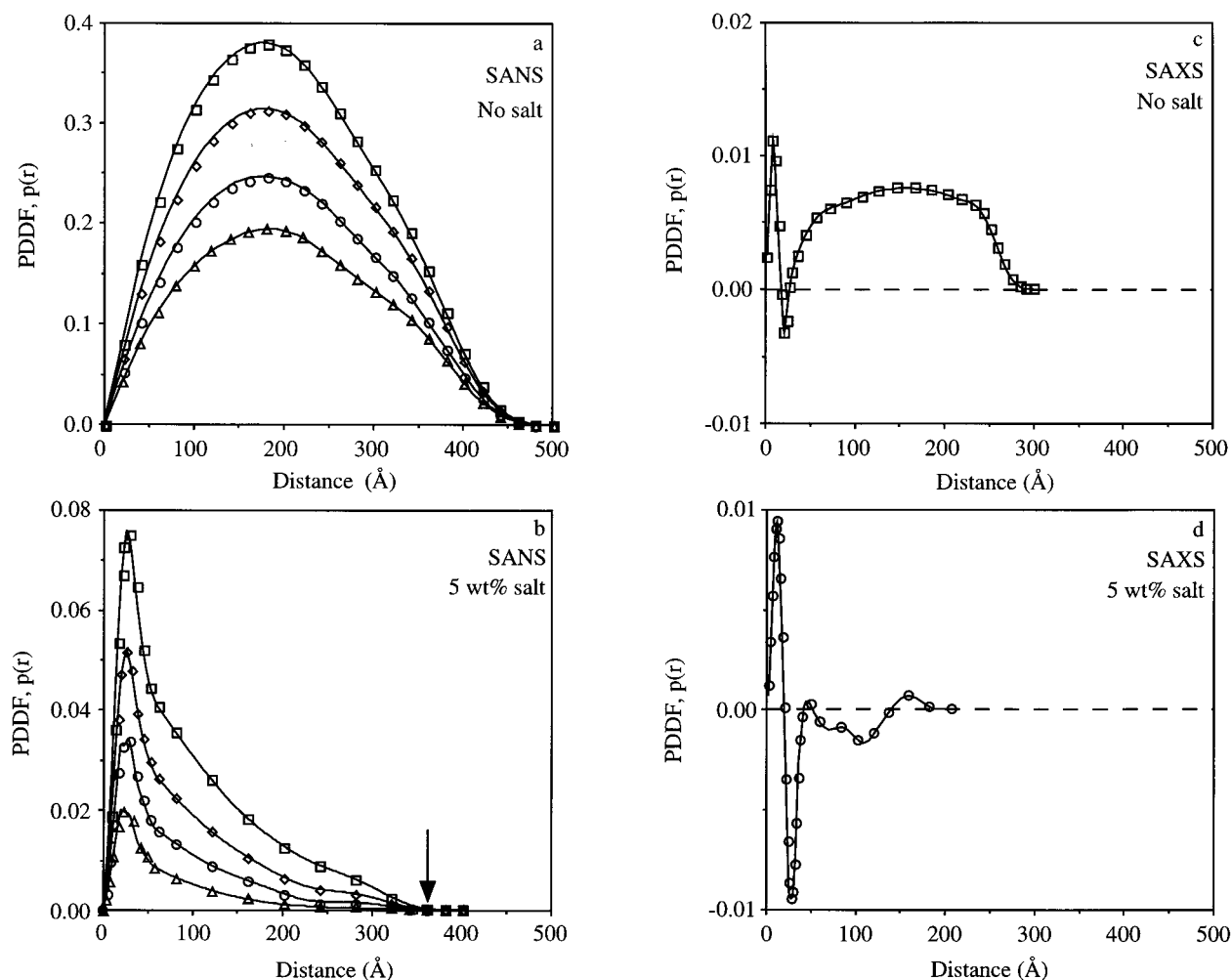


Figure 7. The pair distance distribution functions ($p(r)$) obtained from the indirect Fourier transformation of the intensities in Figures 3–6. (a) PDDFs from the SANS spectra in Figure 3. (b) PDDFs from the SANS spectra in Figure 4. The arrow indicates the approximate length of the cylindrical micelle. Symbols in parts a and b give the fractions of d-SOS as 25% d-SOS (\square), 50% d-SOS (\diamond), 75% d-SOS (\circ), and 100% d-SOS (\triangle). (c) PDDF from the SAXS spectra in Figure 5. (d) PDDF from the SAXS spectra in Figure 6.

In summary, direct analysis of the SANS results (Figures 3 and 4) provides model-independent evidence for the transition from vesicles to micelles upon the addition of NaBr. Analysis of the SAXS results without salt (Figure 5) clearly indicates the existence of planar aggregates, consistent with the findings of SANS. With added salt, the analysis of the SAXS curve (Figure 6) is obscured by a coincidental contrast matching of the aggregate and solvent. Further analysis of this sample will be carried out using the cylindrical geometry indicated by the SANS measurements.

Cross-Sectional PDDF ($p_x(r)$). Once the geometry of the aggregate is established, special transformations²⁰ (eqs 5 and 7) allow calculation of the cross-sectional PDDF, $p_x(r)$ ($x = c$ for cylindrical geometry and t for planar geometry). The $p_x(r)$ are useful because the r value for which $p_x(r) = 0$ provides an estimate of the maximum cross-sectional dimension of the aggregate. Figure 8a–d shows the cross-sectional PDDF curves calculated from the scattered intensities in Figures 3–6 and the PDDFs given in Figure 7. In each figure the maximum cross-sectional dimension is indicated by the arrow. The maximum dimension increases from 30 ± 2 to 37 ± 2 Å for the vesicle and micelle when measured by SANS and from 32 ± 2 to 48 ± 2 Å when measured by SAXS. The trend of increasing dimension as the aggregate morphology changes from planar to cylindrical follows that observed for microemulsions.^{18,19} It is interesting to note that despite having drastically different

scattering spectra, the numerical analysis shows that the dimensions obtained from the $p_x(r)$ functions for the two aggregates are of the same order.

Deconvolution of $p_x(r)$. Deconvolution of $p_x(r)$ produces the contrast profile $\Delta\rho_x(r)$ normal to the interface. The contrast curves are analyzed to obtain two characteristic cross-sectional dimensions, r_c and r_w . r_c is the distance from the point of symmetry ($r = 0$) to the core–headgroup interface and defines the size of the hydrocarbon core. r_w is the distance from the point of symmetry to the point where $\Delta\rho_x(r)$ attains a constant value of zero and defines the maximum extent of the aggregate. The region between r_c and r_w contains the surfactant headgroups. Figure 9 shows the contrast profiles obtained for the vesicle and micellar samples from both SANS (100% d-SOS sample) and SAXS as calculated from the cross-sectional PDDFs in Figure 8. The resolution of the SANS experiments made it difficult to compare the results from the different levels of d-SOS, and therefore we chose to only report the results for one sample. The dimensions r_c and r_w are summarized in Table 1.

As a final conformation for the assumption for cylindrical or planar geometry, the $p_x(r)$ curves calculated by a convolution square of $\Delta\rho_x(r)$ obtained from the SAXS measurements are plotted in Figure 8c,d along with the $p_x(r)$ obtained from the indirect Fourier transformation procedure. Excellent agreement is seen for the planar geometry. The cylindrical geometry

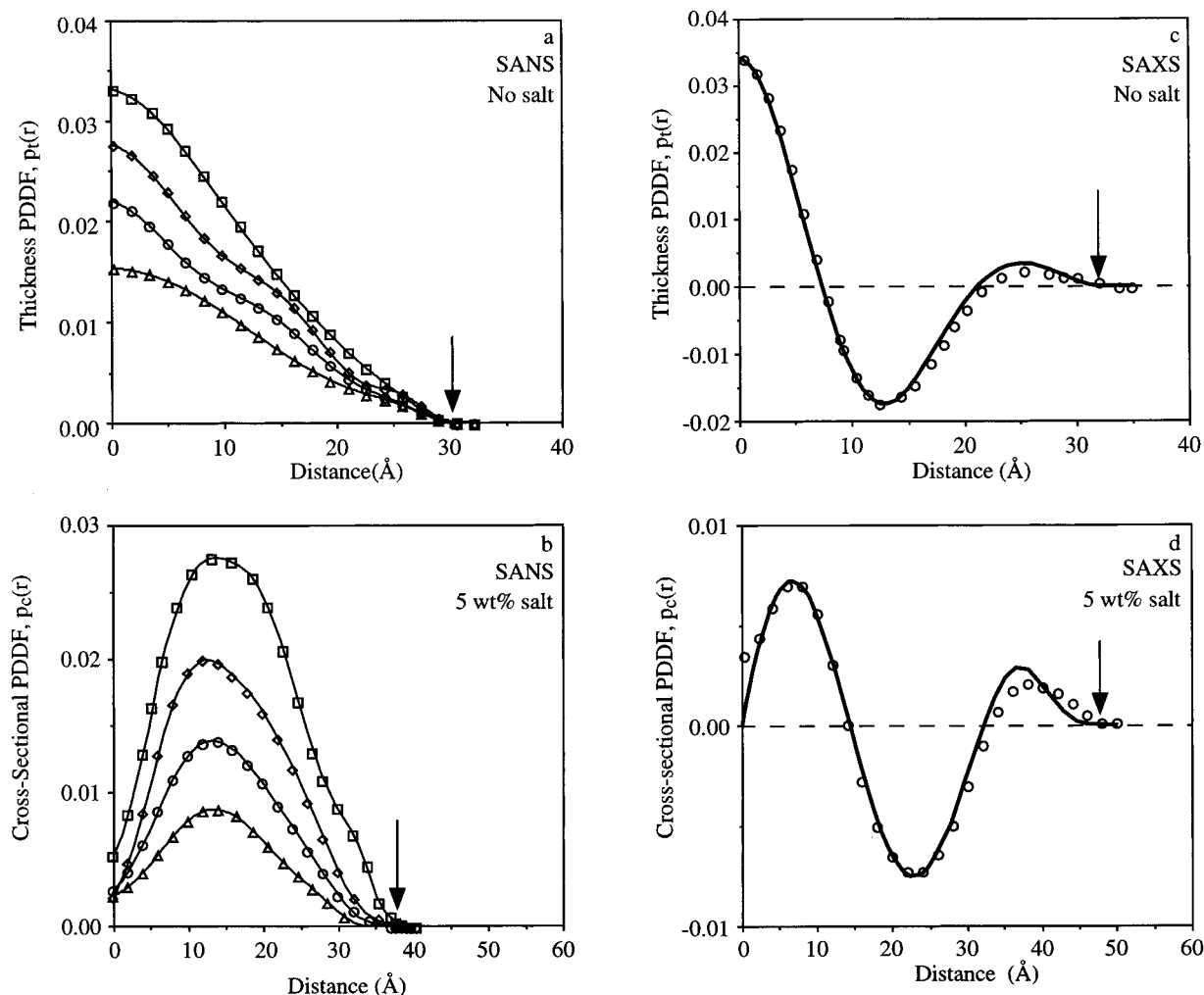


Figure 8. Cross-sectional PDDFs ($p_x(r)$) calculated from the corresponding intensity spectra (Figures 3–6) using either eq 5 or 7 depending on the geometry. (a) Thickness PDDFs for the vesicle calculated from the SANS spectra. (b) Cross-sectional PDDFs for the micelle calculated from the SANS spectra. Symbols in parts a and b give the fractions of d-SOS as 25% d-SOS (\square), 50% d-SOS (\diamond), 75% d-SOS (\circ), and 100% d-SOS (\triangle). (c) Thickness PDDF for the vesicle calculated from the SAXS spectra. (d) Cross-sectional PDDF for the micelle calculated from the SAXS spectra. The solid lines in c and d represent the PDDF calculated by a convolution square of the density profiles in Figure 9c,d. The maximum cross-sectional dimension of the aggregate is indicated by the arrow in each part.

displays reasonably good agreement considering the low overall contrast in the sample.

Discussion

Without the benefit of a priori assumptions about the aggregate structure, the indirect Fourier analysis produces the overall structure and contrast profile of the aggregate, which in turn provides a direct way to determine the dimensions of the aggregate cross section. Since the experimental techniques of SAXS and SANS are sensitive to different physical properties, the contrast profiles are noticeably different, yet must contain the same structural information. A direct comparison of the contrast profiles and subsequent cross-sectional dimensions obtained is shown in Figure 9.

Figure 9a shows the contrast profiles from SANS (filled circles) and SAXS (filled squares) for the vesicle sample. The accurate determination of r_c and r_w from the contrast profiles is essential for the success of the method and for comparison to theoretical predictions. In certain instances the use of one technique over the other may be necessary to obtain the most accurate information. The advantage of using SAXS is evident from the shape of the contrast profile. The electron density of the hydrocarbon chains is lower than the solvent (defined as

$\Delta\rho_t(r) = 0$) while the electron density of the headgroups is higher than the solvent. This requires that $\Delta\rho_t(r)$ be negative for $0 < r < r_c$ and positive for $r_c < r < r_w$. Distances greater than r_w are outside the aggregate and $\Delta\rho_t(r) = 0$. r_c can be clearly identified as the point where the contrast changes sign. Determining r_c from the SANS profile is more ambiguous. Similar to SAXS, the hydrocarbon tails have a lower scattering length density than the solvent, so $\Delta\rho_t(r)$ is negative for $0 < r < r_c$. Unlike the electron density, however, the neutron scattering length density of the headgroups is also lower than the solvent so there is no change in sign of $\Delta\rho_t(r)$ at the edge of the headgroup region. Instead, $\Delta\rho_t(r)$ gradually decreases from the core value to zero in the range of $r_c < r < r_w$. The best estimate for r_c is given by the value of r at which $\Delta\rho_t(r)$ begins to decrease. Table 1 shows that nearly the same structural dimensions are obtained from both experiments despite the ambiguity in defining r_c from SANS.

Figure 9b shows the contrast profiles for the micelle sample calculated from SANS (open circles) and SAXS (open squares). In this case, the values of r_c and r_w indicated by SAXS are 5 Å larger than the corresponding SANS values. Given the discussion above, it would seem likely that the SAXS measurements are more reliable, but in this case the analysis is confounded

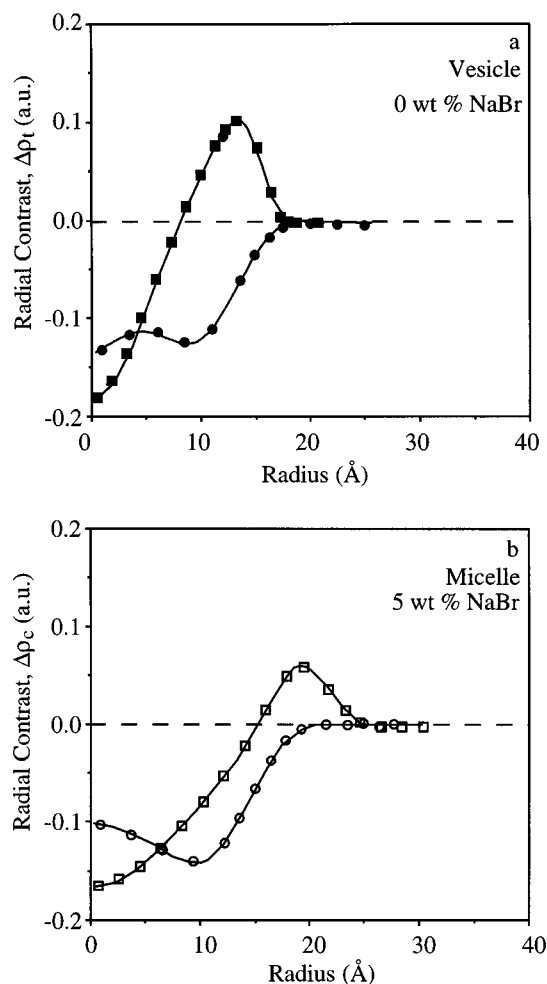


Figure 9. Comparison of the contrast profiles obtained for the vesicle and rodlike micelle geometries as determined from SANS (100% d-SOS) and SAXS experiments. In all cases, zero contrast represents the solvent. (a) Contrast profiles for the vesicle sample from SANS (●) and SAXS (■). (b) Contrast profiles for the micelle sample from SANS (○) and SAXS (□).

TABLE 1: Characteristic Dimensions Calculated from the Contrast Profiles^a

	r_c (Å)	r_w (Å)
vesicle		
SANS	9 ± 1	17 ± 1
SAXS	8 ± 1	18 ± 1
micelle		
SANS	$10-11 \pm 1$	21 ± 1
SAXS	14 ± 2	24 ± 1

^a Errors in the values of r_c and r_w indicate the resolution to which the density profiles can be interpreted.

by the high electrolyte concentration (5 wt % NaBr) in the sample. The high electron density of the electrolyte increases the overall solvent electron density and moves the apparent values of r_c and r_w to larger values. This shift is caused both by the increased solvent mass density and by the higher electron density of the counterions. Thus, the crossing of zero $\Delta\rho_c$ in this case does not correspond to the same place in the surfactant molecule as for the situation in the absence of salt. In addition, the shell of counterions influences determination of r_w . Recall the increase in solvent density also inhibited the analysis of the SAXS data by obscuring the determination of the aggregate geometry from the PDDF (Figure 7d). The effect of the electrolyte on the neutron scattering length density of the solvent

is much less pronounced and therefore does not encumber the analysis of the contrast profile.

The ability to obtain accurate information about the dimensions of the aggregate core and headgroup region from the contrast profile provides an excellent opportunity for comparison with theoretical calculations of the cell model. The model results for a vesicle formed at the same composition explored by SANS and SAXS can be used to calculate the theoretical contrast profile.

The values of r_c and r_w needed to determine the contrast profile are calculated from the model results. r_c is obtained from the optimum half-thickness of the bilayer (11 Å) given by the model. In the model, the half-thickness is the distance from the bilayer midplane to the center of methyl group closest to the headgroup. Assuming that this group is not incorporated in the core, r_c is defined as the half-thickness less the length of a C–C bond. The value of r_w is calculated from the half-thickness plus the average distance the headgroup extends from the first methyl group (1.8 Å for CTAB and 3.6 Å for SOS). The contrast in each region is calculated using known coherent scattering densities²⁶ and molecular volumes.

The neutron scattering contrast profile calculated from the cell model for the lamellar structure (filled circles) is shown in Figure 10a along with that determined experimentally (Figure 9) from IFT. Recently, Schurtenberger and Pedersen et al.^{27,28} have shown theoretically and experimentally that density profiles can be calculated for cylindrical micelles on absolute scale using the IFT method. Their swollen reverse lecithin micelles have a much higher overall contrast and a larger dimension than do the structures studied here, and therefore the spectra were measured at higher resolution. The spectra reported here cannot be analyzed in a similar way, so the contrast profiles from the cell model have been scaled by normalizing the contrast calculated from the model by the contrast calculated by the deconvolution technique at the interior of the bilayer ($r \rightarrow 0$). For simplicity, the theoretical contrast is assumed to be constant in the core and to decay linearly between r_c and r_w . The calculated extent of the hydrocarbon core matches the measured value almost exactly, while in the headgroup region the experimentally determined contrast decreases more slowly and extends to larger distances (larger r_w) than the theoretical profile. The electron density contrast profiles for a lamellar structure calculated from the model (filled circles) and experiment (open circles) are shown in Figure 10b with the numerical value of the contrast from the model again scaled to match the experimental profile at the interior of the bilayer. For comparison, the theoretical electron density profile is approximated by step functions. The theory predicts a modestly larger value of r_c and a smaller value of r_w than observed experimentally.

The experimental contrast profiles indicate that the headgroup region is larger than predicted from the cell model. The increased size of the headgroup region seen experimentally is an indication that the surfactant headgroups are, of course, not fixed at a specific distance from the core (as assumed in the cell model) but instead experience out-of-plane fluctuations and occupy a distribution of headgroup positions. This same type of smearing of the contrast profile has been seen and discussed in the detailed study of the cross-sectional structure of cylindrical and polymer-like micelles.^{27,28} The positioning of the headgroup at the aggregate interface is important in the calculation of several free energy contributions to total aggregation free energy and in particular affects the values of the electrostatic and steric free energies. While the current basic model provides an

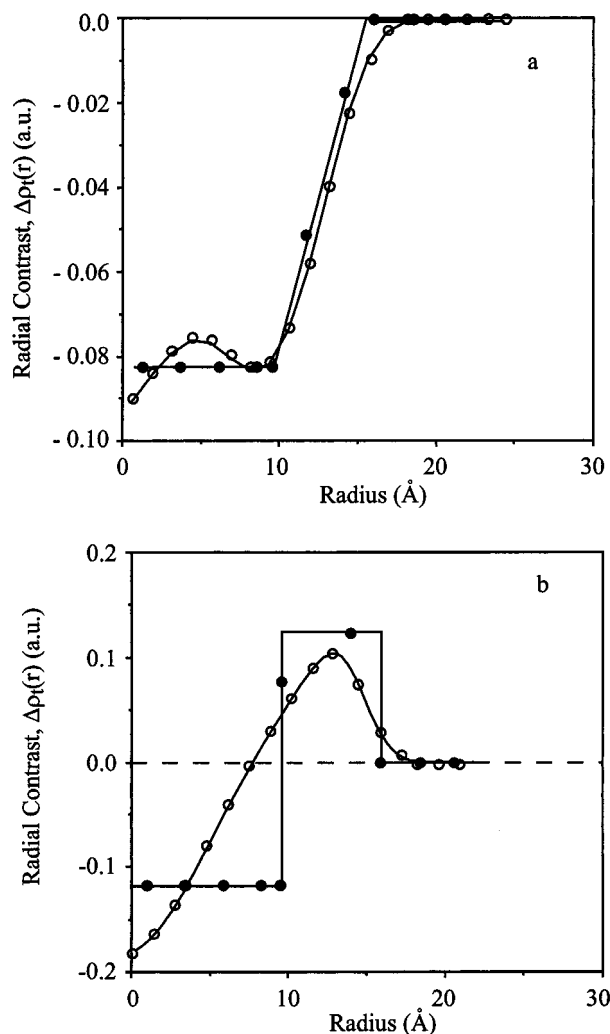


Figure 10. Comparison of the radial contrast profiles for the vesicle sample determined experimentally from the SANS and SAXS intensity spectra and the results of a thermodynamic cell model. (a) Neutron scattering length density profile determined from SANS (○) and the model (●). (b) Electron density profile determined from SAXS (○) and the model (●).

adequate representation of the aggregated structure, these effects need to be included in more accurate models.

Conclusions

Small-angle neutron and X-ray scattering were used in parallel to study the internal and interfacial regions of vesicles and micelles composed of oppositely charged surfactants. An indirect Fourier transform of the scattered data followed by a

deconvolution of the appropriate distance distribution function yields the contrast density profile for the aggregate core. Calculation of the density profiles makes it possible to extract information about the dimensions of the hydrocarbon core and the headgroup region of the aggregates. A comparison of the experimental density profiles for the vesicle geometry with that calculated based on a thermodynamic cell model shows that the model provides a good representation of the vesicle bilayer structure. The enlarged headgroup size indicates that out-of-plane fluctuations of the surfactant molecules are pronounced.

Acknowledgment. We are grateful for the financial support of the National Science Foundation (Grants CTS-9102719 and CTS-9319447) and the Austrian Science Fund (Grant P11778-CHE). We also wish to acknowledge the support of the National Institute of Standards and Technology, U.S. Department of Commerce, in providing the neutron research facilities used in this work.

References and Notes

- (1) Kaler, E. W.; Murthy, A. K.; Rodriguez, B. E.; Zasadzinski, J. A. *Science* **1989**, 245, 1371.
- (2) Lasic, D. D. *J. Colloid Polym. Sci.* **1990**, 140, 302.
- (3) Safran, S. A. *Langmuir* **1991**, 7, 1864.
- (4) Porte, G.; Ligoure, C. *J. Phys. Chem.* **1995**, 99, 4290.
- (5) Bergstrom, M.; Eriksson, J. C. *Langmuir* **1996**, 12, 624.
- (6) Herrington, K. L. Thesis, University of Delaware, 1994.
- (7) Herrington, K. L.; Kaler, E. W.; Miller, D. D.; Zasadzinski, J. A.; Chiruvolu, S. *J. Phys. Chem.* **1993**, 97, 13792.
- (8) Brasher, L. L.; Herrington, K. L.; Kaler, E. W. *Langmuir* **1995**, 11, 4267.
- (9) Nir, S.; Bentz, J.; Duzgunes, J. *Colloid Interface Sci.* **1981**, 84, 266.
- (10) Papahadjopoulos, D.; Vail, W. J.; Newton, C.; Nir, S.; Jacobson, K.; Poste, G.; Lazo, R. *Biochim. Biophys. Acta* **1977**, 465, 579.
- (11) Brasher, L. L. Thesis, University of Delaware, 1996.
- (12) Yuet, P. K.; Blankschtein, D. *Langmuir* **1996**, 12, 3802.
- (13) Stuhmann, H. B. In *Small-Angle X-ray Scattering*; Glatter, O., Kratky, O., Eds.; Academic Press: London, 1982.
- (14) Yacilla, M. T.; Herrington, K. L.; Brasher, L. L.; Kaler, E. W.; Chiruvolu, S.; Zasadzinski, J. A. *J. Phys. Chem.* **1996**, 100, 5874.
- (15) Brasher, L. L.; Kaler, E. W. *Langmuir* **1996**, 12, 6270.
- (16) Glatter, O. *J. Appl. Crystallogr.* **1977**, 10, 415.
- (17) Glatter, O. *J. Appl. Crystallogr.* **1981**, 14, 101.
- (18) Glatter, O.; Strey, R.; Schubert, K.-V.; Kaler, E. W. *Ber. Bunsen-Ges. Phys. Chem.* **1996**, 100, 323.
- (19) Strey, R.; Glatter, O.; Schubert, K.-V.; Kaler, E. W. *J. Chem. Phys.* **1996**, 105, 1175.
- (20) Glatter, O. *J. Appl. Crystallogr.* **1980**, 13, 577.
- (21) Rosen, M. J. *J. Colloid Interface Sci.* **1981**, 79, 587.
- (22) Reid, V. W.; Egham, Longman, G. F.; Cheshire; Heinerth, E.; Dusseldorf *Tenside* **1967**, 4, 292.
- (23) Glatter, O. *J. Appl. Crystallogr.* **1979**, 12, 166.
- (24) Schurtenberger, P.; Cavaco, C. *J. Phys. Chem.* **1994**, 98, 5481.
- (25) Pedersen, J. S.; Schurtenberger, P. *Macromolecules* **1996**, 29, 7602.
- (26) Bacon *Neutron Diffraction*, 3rd ed.; Clarendon: Oxford, UK, 1976.
- (27) Pedersen, J. S.; Schurtenberger, P. *J. Appl. Crystallogr.* **1996**, 29, 646.
- (28) Schurtenberger, P.; Jerke, G.; Cavaco, C. *Langmuir* **1996**, 12, 2433.